

# Elastic Constitutive Relationship of Metallic Materials Containing Grain Shape

Zhiwen Lan <sup>1</sup>, Hanjie Shao <sup>1</sup>, Lei Zhang <sup>2</sup>, Hong Yan <sup>2</sup> , Mojia Huang <sup>1</sup> and Tengfei Zhao <sup>3,\*</sup> 

<sup>1</sup> Institute of Engineering Mechanics, Nanchang University, 999 Xuefu Avenue, Nanchang 330031, China

<sup>2</sup> College of Architectural Engineering and Planning, Jiujiang University, 551 Qianjin East Road, Jiujiang 332005, China

<sup>3</sup> College of City Construction, Jiangxi Normal University, 99 Ziyang Avenue, Nanchang 330022, China

\* Correspondence: 005539@jxnu.edu.cn

**Abstract:** The grain shape and orientation distribution of metal sheets at mesoscales are usually irregular, which has an impact on the elastic properties of metal materials. A grain shape function (GSF) is constructed to represent the shape of grains. The expansion coefficient of GSF on the basis of the Wigner D function is called the shape coefficient. In this paper, we study the influence of average grain shape on the elastic constitutive relation of orthogonal polycrystalline materials, and obtain a new expression of the elastic constitutive relation of polycrystalline materials containing grain shape effects. The seven string method is proposed to fit the shape of irregular grains. Experiments show that the GSF can better describe the shape of irregular grains. Using the microscopic images of the grains, we carried out the experimental measurement of micro and macrostrain at grain scale. The experimental results show that the grain shape parameter (slenderness ratio) is consistent with the theoretical results of the material macroscopic mechanical properties.

**Keywords:** grain shape function; elastic constitutive; seven string method; microscopic images; experimental measurement



**Citation:** Lan, Z.; Shao, H.; Zhang, L.; Yan, H.; Huang, M.; Zhao, T. Elastic Constitutive Relationship of Metallic Materials Containing Grain Shape. *Crystals* **2022**, *12*, 1768. <https://doi.org/10.3390/cryst12121768>

Academic Editor: Pavel Lukáč

Received: 7 November 2022

Accepted: 1 December 2022

Published: 5 December 2022

**Publisher's Note:** MDPI stays neutral with regard to jurisdictional claims in published maps and institutional affiliations.



**Copyright:** © 2022 by the authors. Licensee MDPI, Basel, Switzerland. This article is an open access article distributed under the terms and conditions of the Creative Commons Attribution (CC BY) license (<https://creativecommons.org/licenses/by/4.0/>).

## 1. Introduction

The constitutive relation of metal materials reflects the law of the change of stress with strain under certain deformation conditions. The grains of polycrystalline metal materials contain such microstructure information as grain orientation, grain shape, grain size, and grain boundary distribution [1–5]. The microstructure information reflects the micro structure characteristics of polycrystals, and affect the macro elastic and plastic mechanical properties of polycrystalline materials.

General constitutive theoretical models, such as the Miller [6] model, Walker [7] model, Bonder Partom [8] model, Chaboche [9] model, and Sadovskii model [10], have the following common features [11] despite their various forms: the theoretical basis of each equation is the basic law of thermodynamics. The strain of any point in the material can be regarded as the sum of elastic strain and inelastic strain. The elastic deformation conforms to Hooke's law, and the inelastic deformation conforms to the flow equation. The mechanical properties of materials are determined by two completely independent basic internal variables, i.e., isotropic hardening of the internal variable and kinematic hardening of the internal variable. The above macro phenomenological metal constitutive relation theory is based on macro phenomena and simulates macro mechanical behavior to determine parameters. The equations obtained are often semi theoretical and semi empirical, and the morphology and changes of material damage cannot be understood from the fine and micro structure levels. Therefore, these studies are difficult to go deep into the nature of metal material deformation.

Many studies [12–16] believe that among the micro structural characteristics of metallic materials, the macro elastic constitutive relationship of polycrystalline metallic materials

is mainly affected by the grain orientation distribution. Guenoun et al. [17] followed the grain orientation during in situ crystallization experiments with a fine time resolution. Tang et al. [18] investigated the anisotropic hardness, elastic modulus, and dislocation behavior of AlN grains by Berkovich nanoindentation. Şahin et al. [19] studied the limiting role of grain domain orientation on the modulus and strength of aramid fibers. Tang et al. [20] described the constitutive relation of individual grains in the micro-scale reconstructed models with the single-crystal-scale plasticity model. Gu et al. [21] proposed a method considering grain size and shape effects based on the classical crystal plasticity finite element method. Trusov et al. [22] analyzed the kinematic relations and constitutive laws in crystal plasticity in the case of elastic deformation. Lakshmanan et al. [23] presented a computational framework to include the effects of grain size and morphology in the crystal plasticity. Agius et al. [24] incorporated a length scale dependence into classical crystal plasticity simulations, and the effectiveness of the method was proved by experiments. The grain orientation distribution is expressed by the ODF function [25,26], and the stress distribution of single grains presented obvious orientation dependence during deformation [27]. The relationship between material texture coefficient and the elastic constitutive relationship can reflect the influence of grain orientation distribution on the elastic constitutive relationship. Equations (1) and (2) give the single-crystal-scale plasticity model and polycrystal-scale plasticity model [18,28–38].

$$\left. \begin{aligned} \hat{\sigma}^e &= \mathbf{C} : \mathbf{D}^e \\ \hat{\sigma} &= \hat{\sigma}^e - (\mathbf{W}^p \cdot \boldsymbol{\sigma} - \boldsymbol{\sigma} \cdot \mathbf{W}^p) \\ \hat{\sigma} &= \mathbf{C} : \mathbf{D} - \sum_{\alpha=1}^n (\mathbf{C} : \mathbf{P}^{(\alpha)} + \mathbf{B}^{(\alpha)}) \gamma^{(\alpha)} \end{aligned} \right\} \quad (1)$$

$$\begin{aligned} \hat{\sigma} &= \bar{\mathbf{C}} : \left( \mathbf{D} - \sum_{k=1}^{N_2} \sum_{\alpha=1}^{N_1} \bar{\mathbf{C}} : \mathbf{P}^{(\alpha)} \right) \gamma^{(\alpha)} f_k + \sum_{k=1}^{N_2} \sum_{\alpha=1}^{N_1} \mathbf{B}^{(\alpha)} \gamma^{(\alpha)} f_k \\ &= \bar{\mathbf{C}} : \mathbf{D} - \sum_{k=1}^{N_2} \sum_{\alpha=1}^{N_1} (\bar{\mathbf{C}} : \mathbf{P}^{(\alpha)} + \mathbf{B}^{(\alpha)}) \gamma^{(\alpha)} f_k \end{aligned} \quad (2)$$

However, up to now, people have not given the expression of the polycrystalline elastic constitutive relation containing the grain shape effect. The work of this paper is to study the influence of the grain shape parameters of polycrystalline materials on the elastic constitutive relation, and to carry out the parametric study of the grain shape of grain materials.

## 2. Elastic Constitutive Relationship of Metallic Materials Containing Grain Shape Effect

### 2.1. Grain Shape Function and Shape Coefficient Expression

We define polycrystalline  $\Omega \subset \mathbf{R}^3$  as a collection of many small grains  $\Omega_p$  ( $p = 1, 2, \dots, N$ )

$$\Omega = \text{int} \left( \bigcup_{p=1}^N \bar{\Omega}_p \right), \Omega_p \cap \Omega_q = \emptyset, \forall p \neq q \quad (3)$$

where  $p$  is taken from all grains of polycrystals, the grains  $p$  occupy the domain  $\Omega_p$  (open set),  $\bar{\Omega}_p$  is the closed set of  $\Omega_p$  and is the inner product, and  $N$  is the total number of polycrystal grains.

We assume

$$r_p(\mathbf{n}) = |\mathbf{x} - \mathbf{c}_p|, \mathbf{x} \in \partial\Omega_p \quad (4)$$

Equation (4) represents the distance from the center of the crystal grain  $\Omega_p$  to the point  $\mathbf{x} \in \partial\Omega_p$ , where  $d\mathbf{x} \in dx_1 dx_2 dx_3$  and  $\mathbf{n} = (\mathbf{x} - \mathbf{c}_p) / |\mathbf{x} - \mathbf{c}_p|$ ,  $\mathbf{x} \in \partial\Omega_p$ , the plane calculation model is shown in Figure 1. The direction  $\mathbf{n}$  in (4) can be represented by Euler angles  $\alpha$  and  $\beta$ .

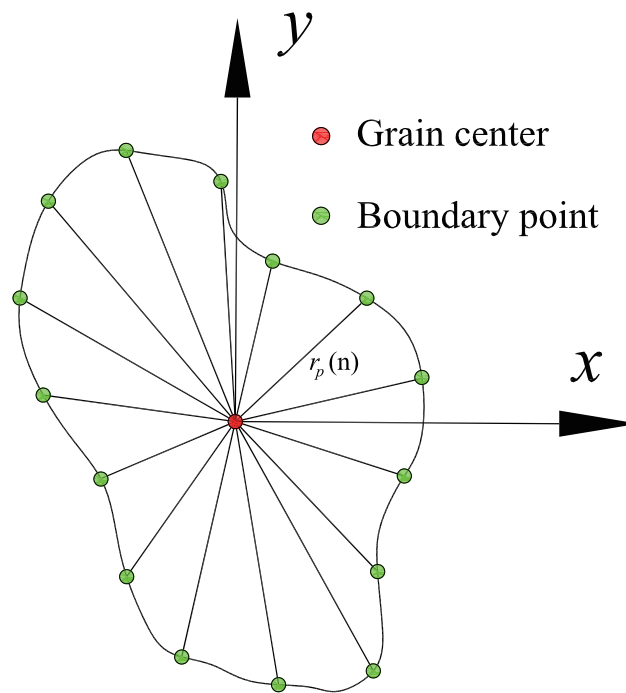


Figure 1. The plane calculation model of the grain.

$$\mathbf{n}(\alpha, \beta) = [\sin \beta \cos \alpha, \sin \beta \sin \alpha, \cos \beta]^T = \mathbf{R}(\alpha, \beta, 0)\mathbf{e}_3 \tag{5}$$

where  $\mathbf{R}(\alpha, \beta, 0)$  is the rotation tensor, and  $\mathbf{e}_3 = [0, 0, 1]^T$ .

The average size  $r(\mathbf{n})$  of crystal grain  $r_p(\mathbf{n})$  in polycrystalline  $\Omega$  is

$$r(\mathbf{n}) = \frac{1}{N} \sum_{p=1}^N r_p(\mathbf{n}) \tag{6}$$

The average shape and size of crystal grains are defined as

$$(\Omega_{cr})_{mean} = \left\{ \mathbf{x} \in \mathbf{R}^3 \mid \mathbf{x} = l(\mathbf{n}) \times [\sin \beta \cos \alpha, \sin \beta \sin \alpha, \cos \beta]^T \right. \\ \left. 0 \leq \alpha < 2\pi, 0 \leq \beta \leq \pi, 0 \leq l(\mathbf{n}) < r(\mathbf{n}) \right\} \tag{7}$$

The elastic constitutive relation is independent of grain size and tiny physical unit, hence

$$\mathfrak{R}(\mathbf{n}(\alpha, \beta)) = \frac{r(\mathbf{n})}{\bar{r}} \tag{8}$$

where  $\bar{r}$  is the average radius of polycrystalline grains, and the GSF can describe the average shape of polycrystalline grains.

$$\bar{r} = \frac{1}{4\pi} \int_0^{2\pi} \int_0^\pi r(\mathbf{n}(\alpha, \beta)) \sin \beta d\beta d\alpha \tag{9}$$

In Equation (8), the GSF  $\mathfrak{R}(\mathbf{n}(\alpha, \beta))$  can be extended to infinite series  $Y_m^l(\alpha, \beta)$  or Wigner D function

$$\mathfrak{R}(\mathbf{n}(\alpha, \beta)) = \mathfrak{R}_{sphere} + \sum_{l=1}^{\infty} \sum_{m=-l}^l \sqrt{\frac{4\pi}{2l+1}} s_{m0}^l Y_m^l(\alpha, \beta) \\ = \mathfrak{R}_{sphere} + \sum_{l=1}^{\infty} \sum_{m=-l}^l s_{m0}^l D_{m0}^l(\mathbf{R}(\alpha, \beta, 0)) \tag{10}$$

where  $\mathfrak{R}_{sphere} = 1$ ,  $s_{m0}^l = (-1)^m (s_{m0}^l)^*$ , and  $s_{m0}^l \in \mathbf{C} (l \geq 1)$  is the shape factor.

The average grain shape is not anisotropic and  $s_{m0}^l = 0$ , the relationship between the ball function and Wigner D function is

$$Y_m^l(\alpha, \beta) = \sqrt{\frac{2l+1}{4\pi}} D_{m0}^l(\mathbf{R}(\alpha, \beta, 0)) \tag{11}$$

According to the orthogonal averaging condition

$$\int_0^{2\pi} \int_0^\pi Y_m^l(\alpha, \beta) (Y_{m'}^{l'}(\alpha, \beta))^* \sin \beta d\beta d\alpha = \delta_{ll'} \delta_{mm'} \tag{12}$$

If  $\|\mathfrak{R}(\mathbf{n}(\alpha, \beta, 0)) - \mathfrak{R}_{sphere}\|$  is a small amount, then the average grain shape is weakly anisotropic. The polycrystalline undergoes a rotation  $\mathbf{Q}$ , and the average shape of grains can be described by a new GSF  $\mathfrak{R}(\mathbf{n}(\alpha, \beta))$ .

$$\begin{aligned} \mathfrak{R}(\mathbf{n}(\alpha, \beta)) &= \mathfrak{R}(\mathbf{Q}^{-1}\mathbf{n}(\alpha, \beta)) = \mathfrak{R}_{sphere} + \sum_{l=1}^{\infty} \sum_{m=-l}^l s_{p0}^l D_{p0}^l(\mathbf{Q}^{-1}\mathbf{R}(\alpha, \beta, 0)) \\ &= \mathfrak{R}_{sphere} + \sum_{l=1}^{\infty} \sum_{m=-l}^l s_{p0}^l \times \sum_{m=-l}^l D_{pm}^l(\mathbf{Q}^{-1}) D_{m0}^l(\mathbf{R}(\alpha, \beta, 0)) \\ &= \mathfrak{R}_{sphere} + \sum_{l=1}^{\infty} \sum_{m=-l}^l \tilde{s}_{m0}^l \times D_{m0}^l(\mathbf{R}(\alpha, \beta, 0)) \end{aligned} \tag{13}$$

where  $\tilde{s}_{m0}^l = \sum_{p=-l}^l s_{p0}^l D_{pm}^l(\mathbf{Q}^{-1})$ .

We assume that the polycrystal is an aggregate of orthorhombic grains, and the shape coefficient of the polycrystal satisfies

$$s_{m0}^l = \sum_{p=-l}^l s_{p0}^l D_{pm}^l(\mathbf{Q}^{-1}), \forall \mathbf{Q}^{-1} \in \{\mathbf{I}, \mathbf{R}(0, \pi, \pi), \mathbf{R}(0, \pi, 0), \mathbf{R}(0, 0, \pi)\} \tag{14}$$

We obtain

$$\begin{cases} s_{m0}^l = (-1)^l s_{\bar{m}0}^l, & m \in \text{even} \\ s_{m0}^l = 0, & m \in \text{odd} \end{cases} \tag{15}$$

Equation (13) holds for all grain aggregates of the orthorhombic system, because

$$\begin{aligned} s_{m0}^l &= \sum_{p=-l}^l s_{p0}^l D_{pm}^l(\mathbf{R}(0, \pi, 0)) \\ &= \sum_{p=-l}^l s_{p0}^l d_{pm}^l(\pi) \\ &= \sum_{p=-l}^l s_{p0}^l (-1)^{l+p} d_{p\bar{m}}^l(0) \\ &= \sum_{p=-l}^l s_{p0}^l (-1)^{l+p} \delta_{p\bar{m}} = s_{\bar{m}0}^l (-1)^{l-m} \end{aligned} \tag{16}$$

$$\begin{aligned} s_{m0}^l &= \sum_{p=-l}^l s_{p0}^l D_{pm}^l(\mathbf{R}(0, 0, \pi)) \\ &= \sum_{p=-l}^l s_{p0}^l d_{pm}^l(0) e^{-im\pi} \\ &= s_{m0}^l \cos(m\pi) \end{aligned} \tag{17}$$

By (13)

$$s_{m0}^l = (-1)^m (s_{\bar{m}0}^l)^* = (-1)^l (s_{m0}^l)^* \tag{18}$$

when the polycrystals have orthogonal symmetry, the dual number  $l$  of the shape coefficient is a real number.

2.2. Elastic Constitutive Relation Considering Average Grain Shape

We assume that the polycrystalline constitutive relation  $\mathbf{C}^{eff}$  depends on ODF and GSF (e.g.,  $\mathbf{C}^{eff} = \mathbf{C}^{eff}(w, \mathfrak{R})$ ), and the objectivity of the material limits the constitutive relation

$$\mathbf{C}^{eff}(w(\mathbf{Q}^{-1}\mathbf{R}), \mathfrak{R}(\mathbf{Q}^{-1}\mathbf{n})) = \mathbf{Q}^{\otimes 4} \mathbf{C}^{eff}(w(\mathbf{R}), \mathfrak{R}(\mathbf{n})), \forall \mathbf{Q} \in \text{SO}(3) \tag{19}$$

$$(\mathbf{Q}^{\otimes 4} \mathbf{A})_{ijkl} = \mathbf{Q}_{im} \mathbf{Q}_{jn} \mathbf{Q}_{kp} \mathbf{Q}_{lq} \mathbf{A}_{mnpq} \tag{20}$$

where, the polycrystalline constitutive relation  $\mathbf{C}^{eff}$  has primary and secondary symmetry, and  $\mathbf{C}^{eff}(w, \mathfrak{R}) = \mathbf{C}^{eff}(c_{mn}^l, s_{m0}^l)$  is expanded into a series with  $c_{mn}^l$  and  $s_{m0}^l$ .

$$\begin{aligned} \mathbf{C}^{eff}(c_{mn}^l, s_{m0}^l) &= \mathbf{C}^{eff}(0, 0) + \sum_{l=1}^{\infty} \sum_n \sum_{m=-l}^l \frac{\partial \mathbf{C}^{eff}(0, 0)}{\partial c_{mn}^l} c_{mn}^l \\ &+ \sum_{l=1}^{\infty} \sum_{m=-l}^l \frac{\partial \mathbf{C}^{eff}(0, 0)}{\partial s_{m0}^l} s_{m0}^l + o(|c_{mn}^l|) + o(|s_{m0}^l|) \end{aligned} \tag{21}$$

If the polycrystal is weak texture (e.g.,  $\|w - w_{iso}\|$  is small), and the average grain shape is weak anisotropy (e.g.,  $\|\mathfrak{R} - \mathfrak{R}_{sphere}\|$  is small), then  $o(|c_{mn}^l|)$  and  $o(|s_{m0}^l|)$  in (21) can be removed, we obtain

$$\mathbf{C}^{eff}(w(\mathbf{R}), \mathfrak{R}(\mathbf{n})) = \mathbf{C}^{eff}(c_{mn}^l, s_{m0}^l) = \mathbf{C}^{(0)} + \mathbf{C}^{(1)}(w(\mathbf{R})) + \mathbf{C}^{(2)}(\mathfrak{R}(\mathbf{n})) \tag{22}$$

where  $\mathbf{C}^{(0)} = \mathbf{C}^{eff}(0, 0)$ .

$$\mathbf{C}^{(1)}(w(\mathbf{R})) = \sum_{l=1}^{\infty} \sum_n \sum_{m=-l}^l \frac{\partial \mathbf{C}^{eff}(0, 0)}{\partial c_{mn}^l} c_{mn}^l \tag{23}$$

$$\mathbf{C}^{(2)}(\mathfrak{R}(\mathbf{n})) = \sum_{l=1}^{\infty} \sum_{m=-l}^l F_{m0}^l s_{m0}^l, F_{m0}^l = \frac{\partial \mathbf{C}^{eff}(0, 0)}{\partial s_{m0}^l} \tag{24}$$

By (19) and (22), we obtain

$$\begin{aligned} \mathbf{C}^{(0)} &= \mathbf{Q}^{\otimes 4} \mathbf{C}^{(0)} \\ \mathbf{C}^{(1)}(w(\mathbf{Q}^{-1}\mathbf{R})) &= \mathbf{Q}^{\otimes 4} \mathbf{C}^{(1)}(w(\mathbf{R})) \\ \mathbf{C}^{(2)}(\mathfrak{R}(\mathbf{Q}^{-1}\mathbf{n})) &= \mathbf{Q}^{\otimes 4} \mathbf{C}^{(2)}(\mathfrak{R}(\mathbf{n})) \end{aligned} \tag{25}$$

For cubic grain orthogonal system, by (25), we obtain the tensor form of  $\mathbf{C}^{(0)}$  and  $\mathbf{C}^{(1)}$  under the change of Voigt symbol.

The isotropic part can be expressed as

$$\begin{aligned} \mathbf{C}^{(0)} &= \lambda \mathbf{B}^{(1)} + 2\mu \mathbf{B}^{(2)} \\ &= \begin{bmatrix} \lambda + 2\mu & \lambda & \lambda & 0 & 0 & 0 \\ \lambda & \lambda + 2\mu & \lambda & 0 & 0 & 0 \\ \lambda & \lambda & \lambda + 2\mu & 0 & 0 & 0 \\ 0 & 0 & 0 & \mu & 0 & 0 \\ 0 & 0 & 0 & 0 & \mu & 0 \\ 0 & 0 & 0 & 0 & 0 & \mu \end{bmatrix} \end{aligned} \tag{26}$$

where  $\lambda$  and  $\mu$  are the undetermined material constants,  $\mathbf{B}_{ijkl}^{(1)} = \delta_{ij}\delta_{kl}$ ,  $\mathbf{B}_{ijkl}^{(2)} = \frac{1}{2}(\delta_{ik}\delta_{jl} + \delta_{il}\delta_{jk})$ .

The anisotropic part can be expressed as

$$\begin{aligned} \mathbf{C}^{(1)} &= c\Phi(w) \\ &= c \begin{bmatrix} -a_2 - a_3 & a_3 & a_2 & 0 & 0 & 0 \\ a_3 & -a_3 - a_1 & a_1 & 0 & 0 & 0 \\ a_2 & a_1 & -a_1 - a_2 & 0 & 0 & 0 \\ 0 & 0 & 0 & a_1 & 0 & 0 \\ 0 & 0 & 0 & 0 & a_2 & 0 \\ 0 & 0 & 0 & 0 & 0 & a_3 \end{bmatrix} \end{aligned} \tag{27}$$

where  $a_1 = -\frac{32\pi^2}{105}(c_{00}^4 + \sqrt{\frac{5}{2}}c_{20}^4)$ ,  $a_2 = -\frac{32\pi^2}{105}(c_{00}^4 - \sqrt{\frac{5}{2}}c_{20}^4)$ ,  $a_3 = \frac{8\pi^2}{105}(c_{00}^4 + \sqrt{70}c_{40}^4)$ , since the polycrystals are cubic crystal orthogonal systems, the texture coefficients  $c_{00}^4$ ,  $c_{20}^4$  and  $c_{40}^4$  are both real numbers [39,40].

In (24), the tensor  $\mathbf{F}_{m0}^l$  satisfies

$$\mathbf{F}_{\bar{m}0}^l = (-1)^m (\mathbf{F}_{m0}^l)^* \tag{28}$$

Hence, the fourth-order tensor  $\mathbf{C}^{(2)}$  is a real number, and by the relationship  $s_{\bar{m}0}^l = (-1)^m (s_{m0}^l)^*$  in (10), we obtain

$$\mathbf{F}_{m0}^l s_{m0}^l + \mathbf{F}_{\bar{m}0}^l s_{\bar{m}0}^l = \mathbf{F}_{m0}^l s_{m0}^l + (\mathbf{F}_{m0}^l s_{m0}^l)^* \tag{29}$$

Combining (24) and (25), we obtain

$$\begin{aligned} \sum_{m=-l}^l s_{m0}^l \mathbf{F}_{m0}^l &= \sum_{m=-l}^l \sum_{p=-l}^l s_{p0}^l D_{pm}^l(\mathbf{Q}^{-1}) \mathbf{F}_{m0}^l \\ &= \sum_{m=-l}^l s_{m0}^l \mathbf{Q}^{\otimes 4} \mathbf{F}_{m0}^l, \forall \mathbf{Q} \in \text{SO}(3) \end{aligned} \tag{30}$$

Equation (30) is applicable to any shape factor  $s_{m0}^l \in \mathbf{C}$ , let  $s_{00}^l \neq 0$  and  $s_{m0}^l = 0$ , we obtain

$$\mathbf{Q}^{\otimes 4} \mathbf{F}_{00}^l = \sum_{m=-l}^l D_{0m}^l(\mathbf{Q}^{-1}) \mathbf{F}_{m0}^l \tag{31}$$

In order to meet the requirement that  $\mathbf{F}_{m0}^l$  holds true for  $\mathbf{Q} \in \text{SO}(3)$ , we assume  $\mathbf{F}_{00}^{(l)} = \mathbf{F}_{00}^l$ , where  $\mathbf{F}^{(l)}$  is a fourth-order tensor satisfying primary and secondary symmetry. We multiply  $(D_{0k}^l(\mathbf{Q}^{-1}))^*$  on both sides of (31) and integrate in  $\text{SO}(3)$  space, then

$$\int_{\text{SO}(3)} \mathbf{Q}^{\otimes 4} \mathbf{F}^{(l)} (D_{0m}^l(\mathbf{Q}^{-1}))^* dg = \sum_{m=-l}^l \int_{\text{SO}(3)} D_{0m}^l(\mathbf{Q}^{-1}) (D_{0k}^l(\mathbf{Q}^{-1}))^* dg \mathbf{F}_{m0}^l \tag{32}$$

$\mathbf{F}_{m0}^l$  can be expressed as

$$\mathbf{F}_{k0}^l = \frac{2l+1}{8\pi^2} \int_{\text{SO}(3)} \mathbf{Q}^{\otimes 4} \mathbf{F}^{(l)} D_{k0}^l(\mathbf{Q}) dg, k \in [0, \pm 1, \pm 2, \dots, \pm l] \tag{33}$$

The component is represented as

$$(\mathbf{F}_{k0}^l)_{mnpq} = \frac{2l+1}{8\pi^2} \int_0^{2\pi} \int_0^\pi \int_0^{2\pi} \mathbf{Q}_{\mu\nu} \mathbf{Q}_{\nu\sigma} \times \mathbf{Q}_{\rho\sigma} \mathbf{Q}_{\rho\tau} \mathbf{F}_{\nu\sigma\tau}^{(l)} D_{k0}^l(\mathbf{Q}) \sin\theta d\psi d\theta d\varphi \tag{34}$$

The fourth-order tensor  $\mathbf{F}^{(l)}$  satisfies the primary and secondary symmetry, and has 21 independent material constants, in (33), the fourth-order tensor  $\mathbf{F}_{m0}^l$  satisfies

$$\mathbf{Q}^{\otimes 4} \mathbf{F}_{m0}^l = \sum_{k=-l}^l (D_{km}^l(\mathbf{Q}))^* \mathbf{F}_{k0}^l \tag{35}$$

We obtain

$$\begin{aligned} \sum_{k=-l}^l (D_{km}^l(\mathbf{Q}))^* \mathbf{F}_{k0}^l &= \sum_{k=-l}^l (D_{mk}^l(\mathbf{Q}^{-1})) \frac{2l+1}{8\pi^2} \times \int_{SO(3)} \mathbf{Q}_1^{\otimes 4} \mathbf{F}^{(l)} D_{k0}^l(\mathbf{Q}_1) dg(\mathbf{Q}_1) \\ &= \frac{2l+1}{8\pi^2} \int_{SO(3)} \mathbf{Q}_1^{\otimes 4} \mathbf{F}^{(l)} \sum_{k=-l}^l D_{mk}^l(\mathbf{Q}^{-1}) D_{k0}^l(\mathbf{Q}_1) dg(\mathbf{Q}_1) \\ &= \frac{2l+1}{8\pi^2} \mathbf{Q}^{\otimes 4} \int_{SO(3)} (\mathbf{Q}^{-1})^{\otimes 4} \mathbf{Q}_1^{\otimes 4} \mathbf{F}^{(l)} D_{m0}^l(\mathbf{Q}^{-1} \mathbf{Q}_1) dg(\mathbf{Q}_1) \\ &= \mathbf{Q}^{\otimes 4} \left( \frac{2l+1}{8\pi^2} \int_{SO(3)} \mathbf{Q}_2^{\otimes 4} \mathbf{F}^{(l)} D_{m0}^l(\mathbf{Q}_2) dg(\mathbf{Q}_2) \right) \\ &= \mathbf{Q}^{\otimes 4} \mathbf{F}_{m0}^l \end{aligned} \tag{36}$$

By  $\mathbf{F}_{k0}^l$  in (33), Equation (30) holds for all shape coefficients  $s_{m0}^l \notin \mathbf{C}$ , hence

$$\begin{aligned} \sum_{k=-l}^l s_{m0}^l \mathbf{Q}^{\otimes 4} \mathbf{F}_{m0}^l &= \sum_{k=-l}^l s_{m0}^l \left[ \sum_{p=-l}^l (D_{mk}^l(\mathbf{Q}))^* \mathbf{F}_{p0}^l \right] \\ &= \sum_{p=-l}^l s_{p0}^l \sum_{m=-l}^l (D_{mp}^l(\mathbf{Q}))^* \mathbf{F}_{m0}^l \\ &= \sum_{m=-l}^l \left( \sum_{p=-l}^l s_{p0}^l D_{pm}^l(\mathbf{Q}^{-1}) \right) \mathbf{F}_{m0}^l \end{aligned} \tag{37}$$

In the rectangular coordinate system, the rotation tensor  $\mathbf{Q}$  can be represented by a linear combination of Wigner D function  $D_{mk}^l(\mathbf{Q})$  ( $l = 1$ ) [41–43], rewriting each component of tensor  $\int_{SO(3)} \mathbf{Q}^{\otimes 4} \mathbf{F}^{(l)} D_{k0}^l(\mathbf{Q}) dg$  [39] as a linear combination of integral  $\int_{SO(3)} D_{qr}^p(\mathbf{Q}) D_{k0}^l(\mathbf{Q}) dg$  ( $0 \leq p \leq 4, l \geq 1$ ). Using the orthogonality of Wigner D function, we obtain

When  $l \geq 5$

$$\mathbf{F}_{k0}^l = \frac{2l+1}{8\pi^2} \int_{SO(3)} \mathbf{Q}^{\otimes 4} \mathbf{F}^{(l)} D_{k0}^l(\mathbf{Q}) dg = 0 \tag{38}$$

By (38), we can write  $\mathbf{C}^{(2)}(\mathfrak{R}(\mathbf{n}))$  in (24) as

$$\mathbf{C}^{(2)}(\mathfrak{R}(\mathbf{n})) = \sum_{l=1}^4 \sum_{m=-l}^l \mathbf{F}_{m0}^l s_{m0}^l \tag{39}$$

By integrating, we obtain

$$\begin{aligned} \sum_{m=-1}^1 \mathbf{F}_{m0}^1 s_{m0}^1 &= 0 \\ \sum_{m=-2}^2 \mathbf{F}_{m0}^2 s_{m0}^2 &= s_1 \Theta_1(\mathfrak{R}) + s_2 \Theta_2(\mathfrak{R}) \\ \sum_{m=-3}^3 \mathbf{F}_{m0}^3 s_{m0}^3 &= 0 \\ \sum_{m=-4}^4 \mathbf{F}_{m0}^4 s_{m0}^4 &= s_3 \Theta_3(\mathfrak{R}) \end{aligned} \tag{40}$$

where

$$\begin{aligned}
s_1 &= \frac{1}{42} (\mathbf{F}_{1111}^{(2)} + \mathbf{F}_{2222}^{(2)} - 2\mathbf{F}_{3333}^{(2)} + 2\mathbf{F}_{2233}^{(2)} + 2\mathbf{F}_{1133}^{(2)} - 4\mathbf{F}_{1122}^{(2)} - 3\mathbf{F}_{2323}^{(2)} - 3\mathbf{F}_{3131}^{(2)} + 6\mathbf{F}_{1212}^{(2)}) \\
s_2 &= \frac{1}{42} (\mathbf{F}_{1111}^{(2)} + \mathbf{F}_{2222}^{(2)} - 2\mathbf{F}_{3333}^{(2)} - 5\mathbf{F}_{2233}^{(2)} - 5\mathbf{F}_{1133}^{(2)} + 10\mathbf{F}_{1122}^{(2)} + 4\mathbf{F}_{2323}^{(2)} + 4\mathbf{F}_{3131}^{(2)} - 8\mathbf{F}_{1212}^{(2)}) \\
s_3 &= \frac{3}{64\pi^2} (3\mathbf{F}_{1111}^{(4)} + 3\mathbf{F}_{2222}^{(4)} + 8\mathbf{F}_{3333}^{(4)} - 8\mathbf{F}_{2233}^{(4)} - 8\mathbf{F}_{1133}^{(4)} + 2\mathbf{F}_{1122}^{(4)} - 16\mathbf{F}_{2323}^{(4)} - 16\mathbf{F}_{3131}^{(4)} + 4\mathbf{F}_{1212}^{(4)})
\end{aligned} \tag{41}$$

$$\begin{aligned}
\Theta_1(\mathfrak{R}) &= \begin{bmatrix} 4s_{00}^2 - 4\sqrt{6}s_{20}^2 & 0 & 0 & 0 & 0 & 0 & 0 \\ 0 & 4s_{00}^2 + 4\sqrt{6}s_{20}^2 & 0 & 0 & 0 & 0 & 0 \\ 0 & 0 & -8s_{00}^2 & 0 & 0 & 0 & 0 \\ 0 & 0 & 0 & -s_{00}^2 + \sqrt{6}s_{20}^2 & 0 & 0 & 0 \\ 0 & 0 & 0 & 0 & -s_{00}^2 - \sqrt{6}s_{20}^2 & 0 & 0 \\ 0 & 0 & 0 & 0 & 0 & -s_{00}^2 - \sqrt{6}s_{20}^2 & 0 \\ 0 & 0 & 0 & 0 & 0 & 0 & 2s_{00}^2 \end{bmatrix} \\
\Theta_2(\mathfrak{R}) &= \begin{bmatrix} 2s_{00}^2 - 2\sqrt{6}s_{20}^2 & 2s_{00}^2 & -s_{00}^2 - \sqrt{6}s_{20}^2 & 0 & 0 & 0 \\ 2s_{00}^2 & 2s_{00}^2 + 2\sqrt{6}s_{20}^2 & -s_{00}^2 + \sqrt{6}s_{20}^2 & 0 & 0 & 0 \\ -s_{00}^2 - \sqrt{6}s_{20}^2 & -s_{00}^2 + \sqrt{6}s_{20}^2 & -4s_{00}^2 & 0 & 0 & 0 \\ 0 & 0 & 0 & 0 & 0 & 0 \\ 0 & 0 & 0 & 0 & 0 & 0 \\ 0 & 0 & 0 & 0 & 0 & 0 \end{bmatrix} \\
\Theta_3(\mathfrak{R}) &= \begin{bmatrix} -b_2 - b_3 & b_3 & b_2 & 0 & 0 & 0 \\ b_3 & -b_1 - b_3 & b_1 & 0 & 0 & 0 \\ b_2 & b_1 & -b_1 - b_2 & 0 & 0 & 0 \\ 0 & 0 & 0 & b_1 & 0 & 0 \\ 0 & 0 & 0 & 0 & b_2 & 0 \\ 0 & 0 & 0 & 0 & 0 & b_3 \end{bmatrix}
\end{aligned} \tag{42}$$

$$b_1 = -\frac{32\pi^2}{105} (s_{00}^4 + \sqrt{\frac{5}{2}}s_{20}^4), \quad b_2 = -\frac{32\pi^2}{105} (s_{00}^4 - \sqrt{\frac{5}{2}}s_{20}^4), \quad b_3 = \frac{8\pi^2}{105} (s_{00}^4 - \sqrt{70}s_{20}^4) \tag{43}$$

By (19), for orthogonal polycrystals, in (41)–(43), the shape coefficients  $s_{00}^2, s_{20}^2, s_{00}^4, s_{20}^4, s_{00}^4, s_{20}^4$  are real numbers. Substitute (40) into (39), and we obtain the anisotropic part of the constitutive relation according to the anisotropy of the average grain shape

$$\mathbf{C}^{(2)}(\mathfrak{R}(\mathbf{n})) = s_1\Theta_1(\mathfrak{R}) + s_2\Theta_2(\mathfrak{R}) + s_3\Theta_3(\mathfrak{R}) \tag{44}$$

If the polycrystals are orthorhombic aggregates of weakly textured cubic grains, and the average grain shape is weakly anisotropic, according to the principle of material objectivity, considering the effects of GSF and grain orientation function ODF, by (22), (42), (43), and (44), we obtain the elastic constitutive relationship  $\mathbf{C}^{eff}$  of polycrystals

$$\mathbf{C}^{eff} = \lambda\mathbf{B}^{(1)} + 2\mu\mathbf{B}^{(2)} + c\Phi(w) + s_1\Theta_1(\mathfrak{R}) + s_2\Theta_2(\mathfrak{R}) + s_3\Theta_3(\mathfrak{R}) \tag{45}$$

where  $\lambda, \mu, c, s_1, s_2$  and  $s_3$  are undetermined material constants, which can be determined by experiment, physical model, or numerical simulation.

### 3. Parameterization and Experiment of Metal Material Grain Shape

On the meso scale, when discussing the relationship between the grain shape and the mechanical properties of metal materials, most of the grain shapes are expressed as ellipses. In fact, the grain shapes of polycrystalline metal materials are very different, and there is no unified shape description method for irregular grains. This section discusses the mathematical description of the grain shape, introduces the parameters that represent the grain shape, uses the digital image analysis method to realize the parametric representation of the evolution of the micro and macrograin shape of metal materials under stress

deformation, and carries out experimental research on the mechanical properties of metal materials containing the grain shape effect.

### 3.1. Extraction of Grain Image

Through the test of several common metal materials (e.g., the low carbon steel, pure copper, and pure aluminum), we found that using pure aluminum sheets can obtain relatively clear grain images, so the grain images analyzed in this paper are taken from a pure aluminum sheet. We process the rolled pure aluminum plate into a dumbbell-shaped sample, conduct high temperature annealing at 600 °C for 30 min, and cool it in the furnace to room temperature. Then we use mixed acid solution (15 mL HF, 15 mL HNO<sub>3</sub>, 25 mL HCl, 25 mL H<sub>2</sub>O) to etch the sample, remove the oxide layer on the surface of pure aluminum plate, and expose the grain structure. These grains can also be used as natural speckles on the sample surface, as shown in Figure 2.

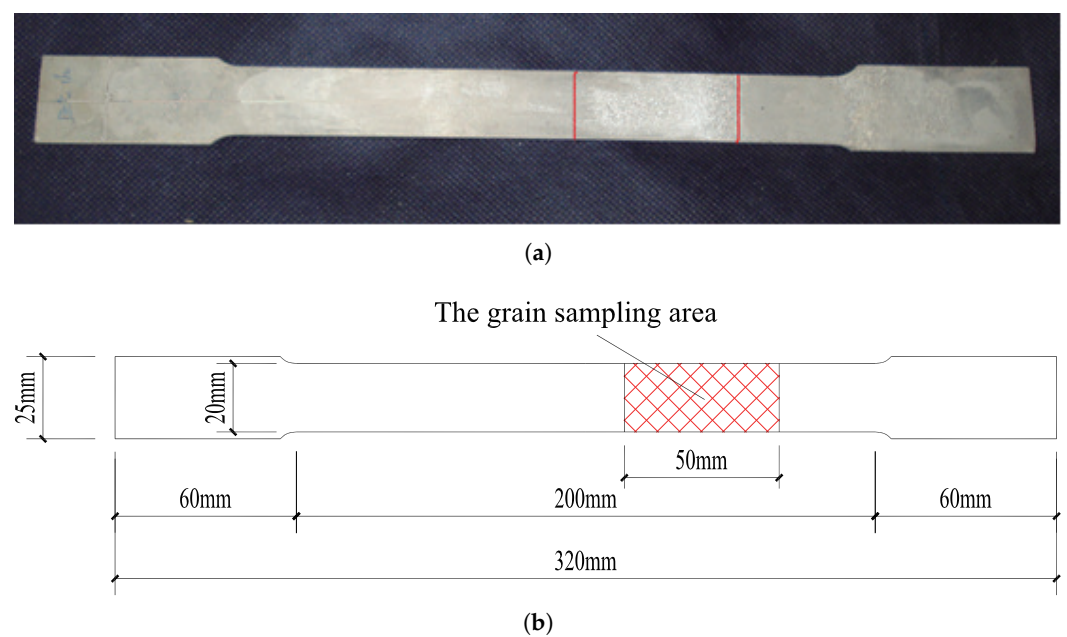


**Figure 2.** (a) The original grain on pure aluminum plate specimen (natural speckle); (b) the dimensions of the plate specimen.

In order to facilitate the research, the following five images (as shown in Figure 3) with clear grain boundaries and easily recognizable grain shapes during loading are selected from a large number of sample grain images, which are marked with GRAB1, GRAB5, GRAB10, GRAB14, and GRAB15, respectively. Three grains with obvious boundary contours are selected from these five grain images for shape parameterization research.

First, we use the 2D Gaussian filtering template to smooth the image, calculate the amplitude and direction of the filtered image gradient, apply non-maximum suppression to the gradient amplitude, find out the local maximum points in the image gradient, set other non-local maximum points to zero to obtain the refined edge, and use the double threshold algorithm to detect and connect the edges, use two thresholds to find each line segment and extend them in two directions to find the fracture at the grain boundary edge, and connect these fractures.

From Figure 3, taking GRAB1 as an example, three grains with clear grain boundaries were selected as the research object, and the boundary diagrams of the three grains under different loads were intercepted by using the aforementioned boundary extraction method, as shown in Figure 4.

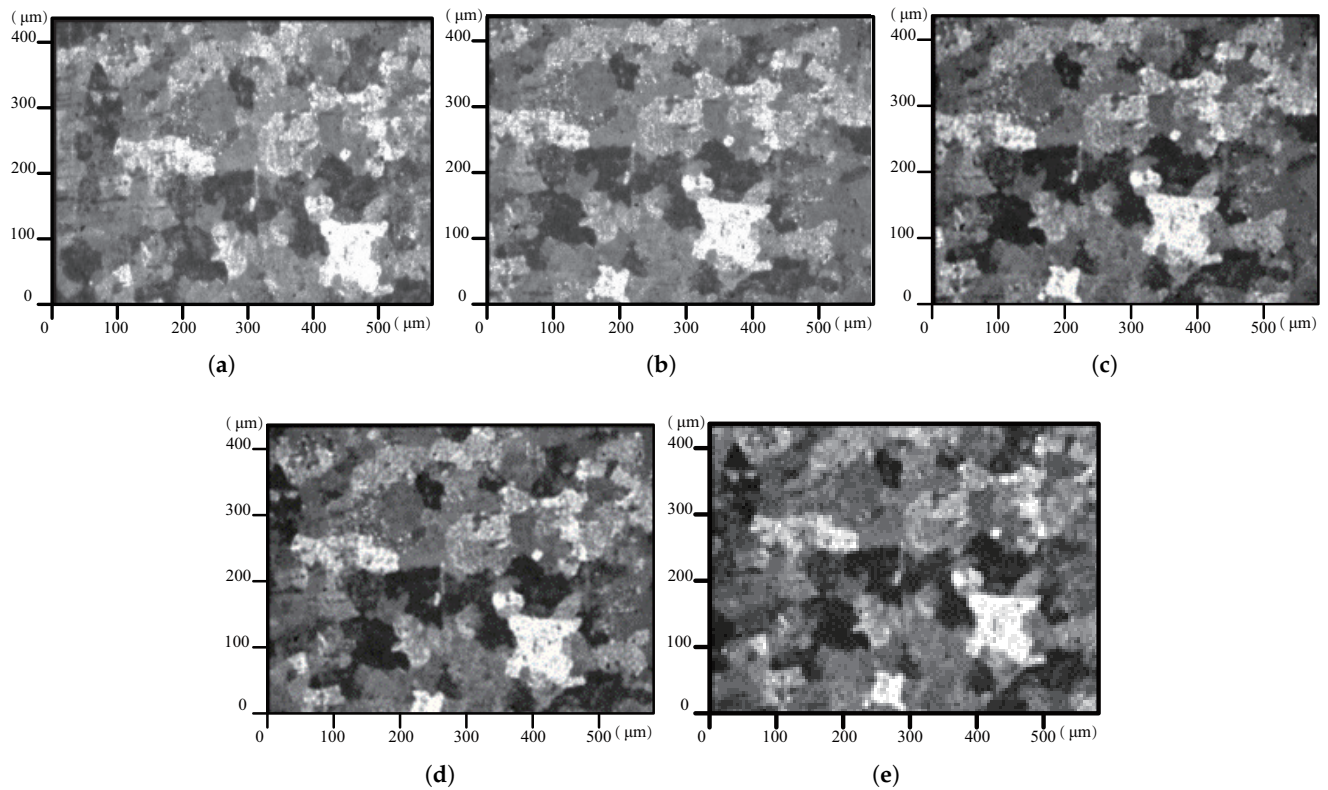


**Figure 3.** The original grain image of pure aluminum plate sample: (a) GRAB 1; (b) GRAB 5; (c) GRAB 10; (d) GRAB 14; (e) GRAB 15.

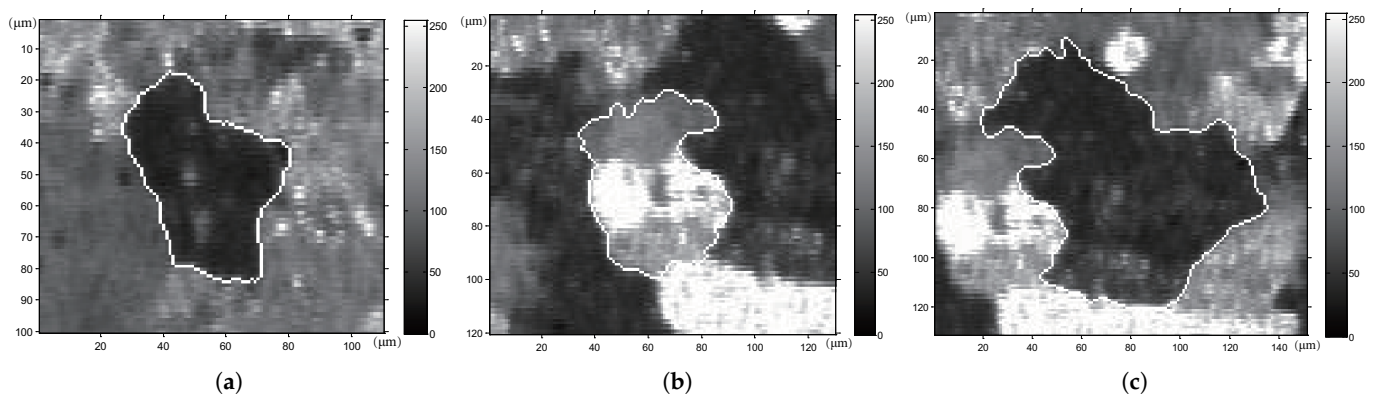


**Figure 4.** The boundary diagram of three grains in GRAB1: (a) grain 1; (b) grain 2; (c) grain 3.

### 3.2. Multi-String Method for Grain Shape Parameterization

The grain shape parameters can be fitted by the external rectangle, ellipse, and the multi-chord method for grain segmentation. By comparison, we find that the external rectangle and ellipse are sometimes not the closest fitting figure to the actual shape of the grain for grains with different shapes, and the multi-chord method for grain segmentation is more accurate and effective for the boundary fitting of irregular grains.

Taking the digital speckle image of grain 1, grain 2, and grain 3 provided in Figure 4 as the data source, and taking the minimum circumscribed rectangle at the edge of the grain as the object, we divide the minimum circumscribed rectangle into eight equal parts in the height and width directions respectively, then we obtain seven strings in the vertical and horizontal directions inside the grain, calculate the length of each string respectively, and take the ratio of the average length of the vertical and horizontal chords as the slenderness

ratio of the grain, i.e., the grain shape parameter. Figure 5 is the schematic diagram of irregular grain boundary multi-chord method fitting.

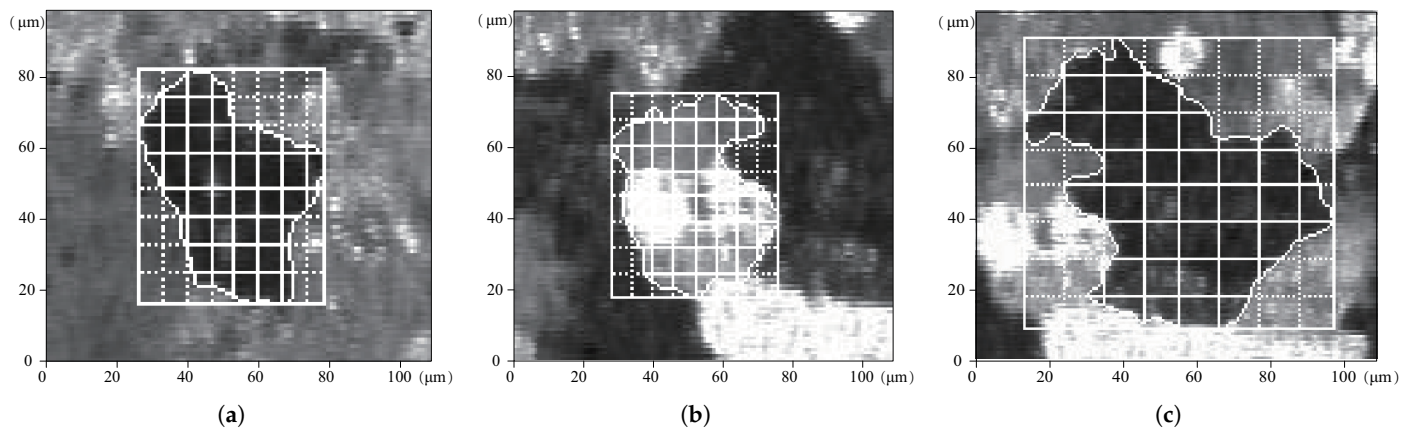


**Figure 5.** The multi-chord fitting of three grain boundaries: (a) grain 1; (b) grain 2; (c) grain 3.

We fit and calculate each chord (solid line part) in each grain in Figure 5. The calculation data and shape parameters are listed in Table 1 according to the number of chords in each grain.

Since the number of chords for dividing grains can be set manually, the appropriate number of chords depends on whether the shape of grains can be truly reflected and the efficiency of calculation. Therefore, this paper analyzes and compares the number of chords in the multi-chord method. Tables 1–3 list the fitting data and corresponding shape parameters of the grain image after grain segmentation with 1, 3, 5, and 7 chords in three grains.

**Table 1.** The multi-chord grain fitting data and shape parameters (grain 1).

Chord Number	1 Chord			3 Chord			5 Chord			7 Chord		
	Grain Image Number	H. <sup>1</sup>	W. <sup>2</sup>	S.R. <sup>3</sup>	H. <sup>1</sup>	W. <sup>2</sup>	S.R. <sup>3</sup>	H. <sup>1</sup>	W. <sup>2</sup>	S.R. <sup>3</sup>	H. <sup>1</sup>	W. <sup>2</sup>
GRAB1	67	45	1.489	65.67	45.33	1.449	67.4	46.4	1.453	68.14	46.71	1.459
GRAB5	69	44	1.568	70	44.67	1.567	68.8	44.2	1.557	70.57	45.13	1.564
GRAB10	70	44	1.591	70.33	44	1.598	70.8	44	1.609	71.28	44.85	1.59
GRAB14	75	41	1.829	75.67	40.67	1.861	75.6	41	1.844	76.11	40.14	1.896
GRAB15	77	40	1.925	77	40.33	1.909	77	40.6	1.897	77.57	39.42	1.968

<sup>1</sup> This is the height of the crystal. <sup>2</sup> This is the width of the crystal. <sup>3</sup> This is the slenderness ratio of the crystal.

**Table 2.** The multi-chord grain fitting data and shape parameters (grain 2).

Chord Number	1 Chord			3 Chord			5 Chord			7 Chord		
	Grain Image Number	H. <sup>1</sup>	W. <sup>2</sup>	S.R. <sup>3</sup>	H. <sup>1</sup>	W. <sup>2</sup>	S.R. <sup>3</sup>	H. <sup>1</sup>	W. <sup>2</sup>	S.R. <sup>3</sup>	H. <sup>1</sup>	W. <sup>2</sup>
GRAB1	51	44	1.159	53	39.67	1.336	53.8	40.7	1.322	53.37	40.93	1.304
GRAB5	56	45	1.244	53	40	1.325	53.6	40.6	1.321	53.73	40.87	1.314
GRAB10	50	46	1.087	51	41	1.244	53.2	40.4	1.317	53.84	40.23	1.338
GRAB14	59	46	1.283	55.33	40.67	1.361	54.4	41.1	1.324	54.33	41.54	1.307
GRAB15	55	45	1.222	55.67	40.33	1.38	55.2	41.7	1.324	55.87	41.67	1.341

<sup>1</sup> This is the height of the crystal. <sup>2</sup> This is the width of the crystal. <sup>3</sup> This is the slenderness ratio of the crystal.

**Table 3.** The multi-chord grain fitting data and shape parameters (grain 3).

Chord Number	1 Chord			3 Chord			5 Chord			7 Chord		
	Grain Image Number	H. <sup>1</sup>	W. <sup>2</sup>	S.R. <sup>3</sup>	H. <sup>1</sup>	W. <sup>2</sup>	S.R. <sup>3</sup>	H. <sup>1</sup>	W. <sup>2</sup>	S.R. <sup>3</sup>	H. <sup>1</sup>	W. <sup>2</sup>
GRAB1	103	109	0.945	106.67	109.33	0.976	102.8	108.6	0.947	103.57	109.17	0.949
GRAB5	105	108	0.972	108	107.67	1.003	106.2	108.2	0.982	104.58	108.71	0.962
GRAB10	108	106	1.019	109.33	106	1.031	108.4	105.8	1.025	109.17	105.14	1.038
GRAB14	111	103	1.078	110.67	103.33	1.071	112.2	102.6	1.094	111.34	102.47	1.087
GRAB15	113	100	1.13	114.33	100	1.143	113	99.2	1.139	114.02	99.42	1.147

<sup>1</sup> This is the height of the crystal. <sup>2</sup> This is the width of the crystal. <sup>3</sup> This is the slenderness ratio of the crystal.

According to the grain shape fitting data in Tables 1–3, we find that the results of grain shape fitting for the same grain under the same load state are different with a different number of split chords. When the number of split chords is 5 and 7, the grain fitting data shows better convergence, which is significantly different from the grain fitting data when the number of split chords is 1 and 3. Theoretically, the more the number of segmenting chords of the grains, the more information reflecting the shape of the grains, and the closer the description of the shape of the irregular grains should be. However, there is a problem of computational efficiency at this time. After comparison, the seven chords can be used as the more appropriate chord number of the multi-chord method for segmenting grains.

### 3.3. Experimental Study on Grain Shape Coefficient

In Section 2, according to the ratio of the arbitrary radius value to the average radius value in the grain, we establish the GSF to describe the average shape of the grain. The GSF can be expanded into infinite series on the basis of Wigner D function, and the expanded coefficients are called grain shape coefficients  $s_{m0}^l$  (Equations (10)–(13)). Equation (10) degenerates to the form of a plane, then

$$r(\theta) = 1 + 2 \sum_{i=1}^4 [a_i \cos(i\theta) + b_i \sin(i\theta)] \quad (46)$$

where  $r(\theta)$  is the shape function of the grain,  $a_i$  and  $b_i$  are the coefficients of the expansion series of the GSF, i.e., the grain shape coefficient.

We select the first loading step G1 of grain 1, find the centroid of the grain through the image analysis technology in Section 3.1, and establish a rectangular coordinate system with the centroid as the coordinate origin (as shown in Figure 6), segment the grain with the seven chord method, and obtain 28 information points at the transverse chord end and vertical chord end on the grain boundary.

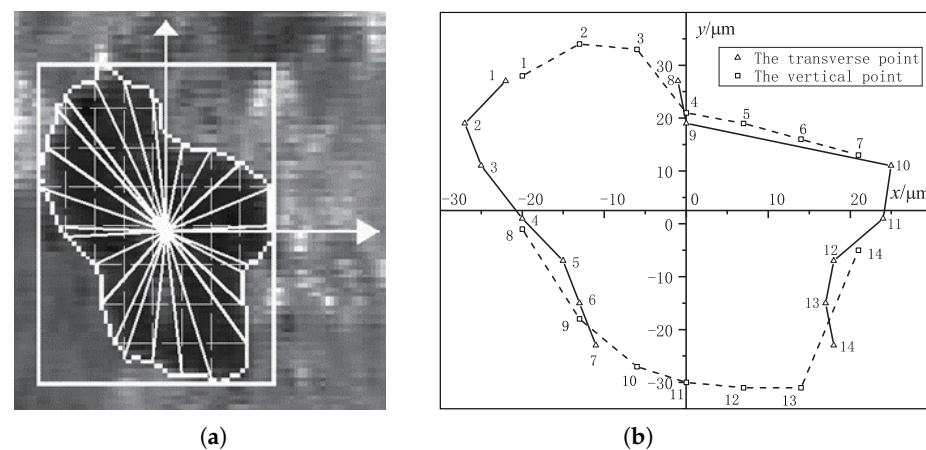


**Figure 6.** (a) The grain 1 (G1) in the rectangular coordinate system; (b) the transverse and vertical points.

Further, we obtain the X and Y coordinate values of the 28 information points, as shown in Tables 4 and 5.

**Table 4.** The coordinates of grain 1 (G1) boundary information points (transverse point).

Point Number	X	Y	Point Number	X	Y
Transverse point 1	−22	27	Transverse point 8	−1	27
Transverse point 2	−27	19	Transverse point 9	0	19
Transverse point 3	−25	11	Transverse point 10	25	11
Transverse point 4	−20	1	Transverse point 11	24	1
Transverse point 5	−15	−7	Transverse point 12	18	−7
Transverse point 6	−13	−15	Transverse point 13	17	−15
Transverse point 7	−11	−23	Transverse point 14	18	−23

**Table 5.** The coordinates of grain 1 (G1) boundary information points (vertical point).

Point Number	X	Y	Point Number	X	Y
Vertical point 1	−20	28	Vertical point 8	−20	−1
Vertical point 2	−13	34	Vertical point 9	−13	−18
Vertical point 3	−6	33	Vertical point 10	−6	−27
Vertical point 4	0	21	Vertical point 11	0	−30
Vertical point 5	7	19	Vertical point 12	7	−31
Vertical point 6	14	16	Vertical point 13	14	−31
Vertical point 7	21	13	Vertical point 14	21	−5

Using the same processing method, each grain has five analysis steps (G1, G5, G10, G14, G15), and we obtain 15 data sheets of three grains. According to the coordinate value of each information point, we calculate the distance  $R$  from the information point to the centroid, the average distance  $\bar{r}$ , and the included angle  $\theta$  between the centroid line of the information point and the X axis. If  $r = R/\bar{r}$ ,  $r$  is the shape function value of the function  $r(\theta)$  corresponding to  $\theta$ . In (46), we can establish

$$\Pi = \sum_{i=1}^{28} [r(\theta_i) - r_i]^2 \quad (47)$$

where  $r(\theta_i)$  is the value of function  $r(\theta)$  when  $\theta = \theta_i$ , and  $r_i$  is the experimental value corresponding to  $\theta = \theta_i$ .

According to  $\frac{\partial \Pi}{\partial a_i} = 0$ ,  $\frac{\partial \Pi}{\partial b_i} = 0$  ( $i = 1 \cdots n$ ,  $n$  is the number of experimental data points), we obtain  $a_i$ ,  $b_i$ .

Using the seven string method, the results of grain 1 shape fitting are obtained as shown in Figure 7. Figure 7a shows the shape function curve of grain 1, and the fitting curve is in good agreement with the experimental data points. Figure 7b reflects the function fitting curve of grain 1 under different loading steps. The five grain curves are not completely coincident, reflecting the changes of grain shape under load. Such fitting results show that the GSF can better describe the shape of irregular grains, where the grain shape coefficients  $a_i$  and  $b_i$  are coefficients of the expansion of the GSF, and different grain shape coefficients correspond to different grain shapes.

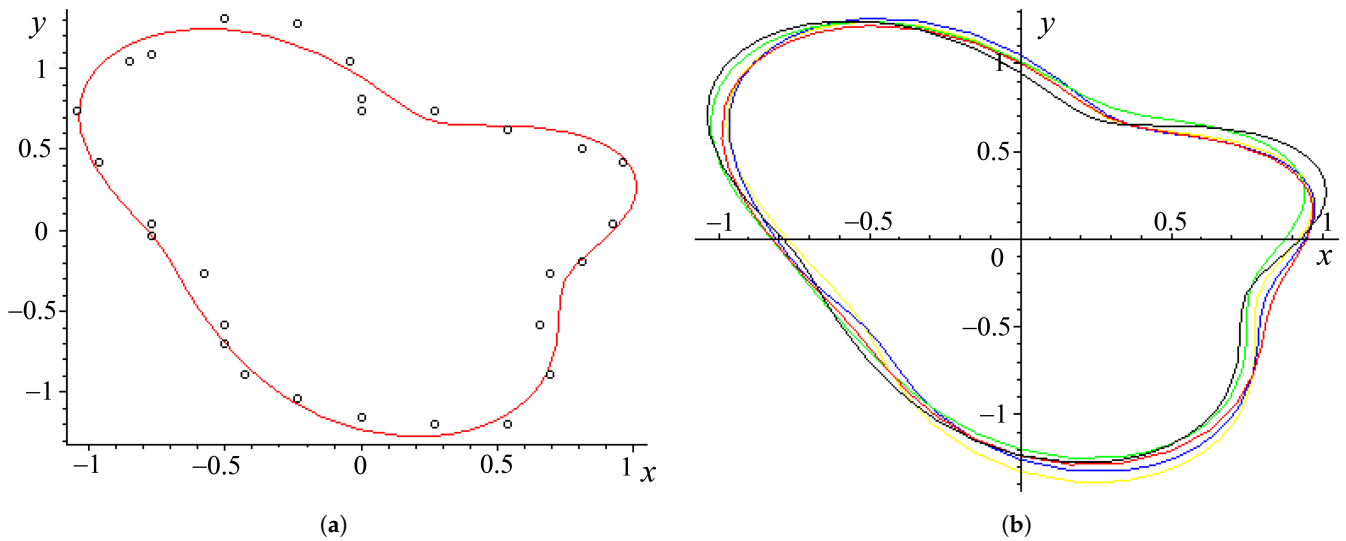


**Figure 7.** (a) The shape function fitting curve of grain; (b) the function fitting curve of grain 1 under different loading steps.

#### 4. Parametric Experimental Study on Grain Shape Evolution

In Section 3, we studied the parametric shape of grains with different shapes in the micro structures of polycrystalline metal materials. In this section, taking the axial tensile deformation experiment of pure aluminum plate as an example, we discussed the micro shape evolution of grains under macro tension from the micro scale of metal grain shape parameters.

Figure 8 shows the local grain diagram in the pure aluminum plate sample. There are a large number of grains with irregular shapes within the grain image range. We selected grains with relatively regular shape and near ellipse as the analysis object of this experimental study. The target grain (red) is shown in Figure 8b.

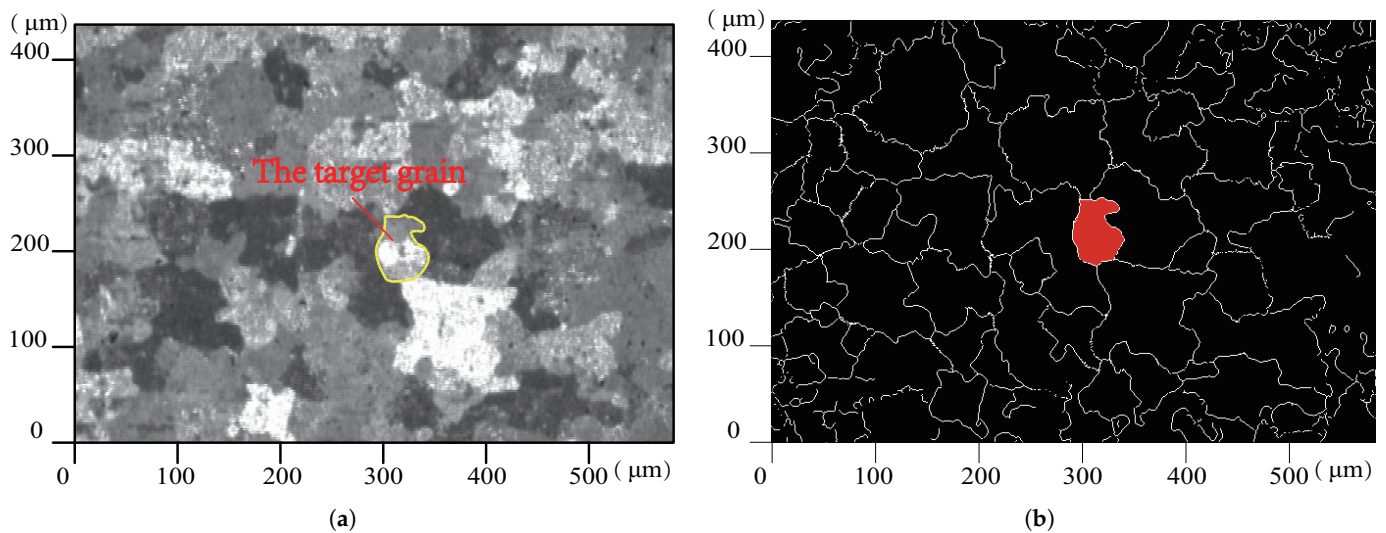


**Figure 8.** (a) The target grain of the grain diagram when  $F = 200$  N; (b) the corresponding boundary diagram.

During the tensile loading of a pure aluminum sheet, the grain distribution on the surface of the sheet is synchronously collected. The loading range is  $0\text{ N} \sim 3800\text{ N}$ . Images are collected every  $200\text{ N}$ . The images collected under various loads are processed, and the corresponding grain boundary diagram is obtained, as shown in Figure 9.

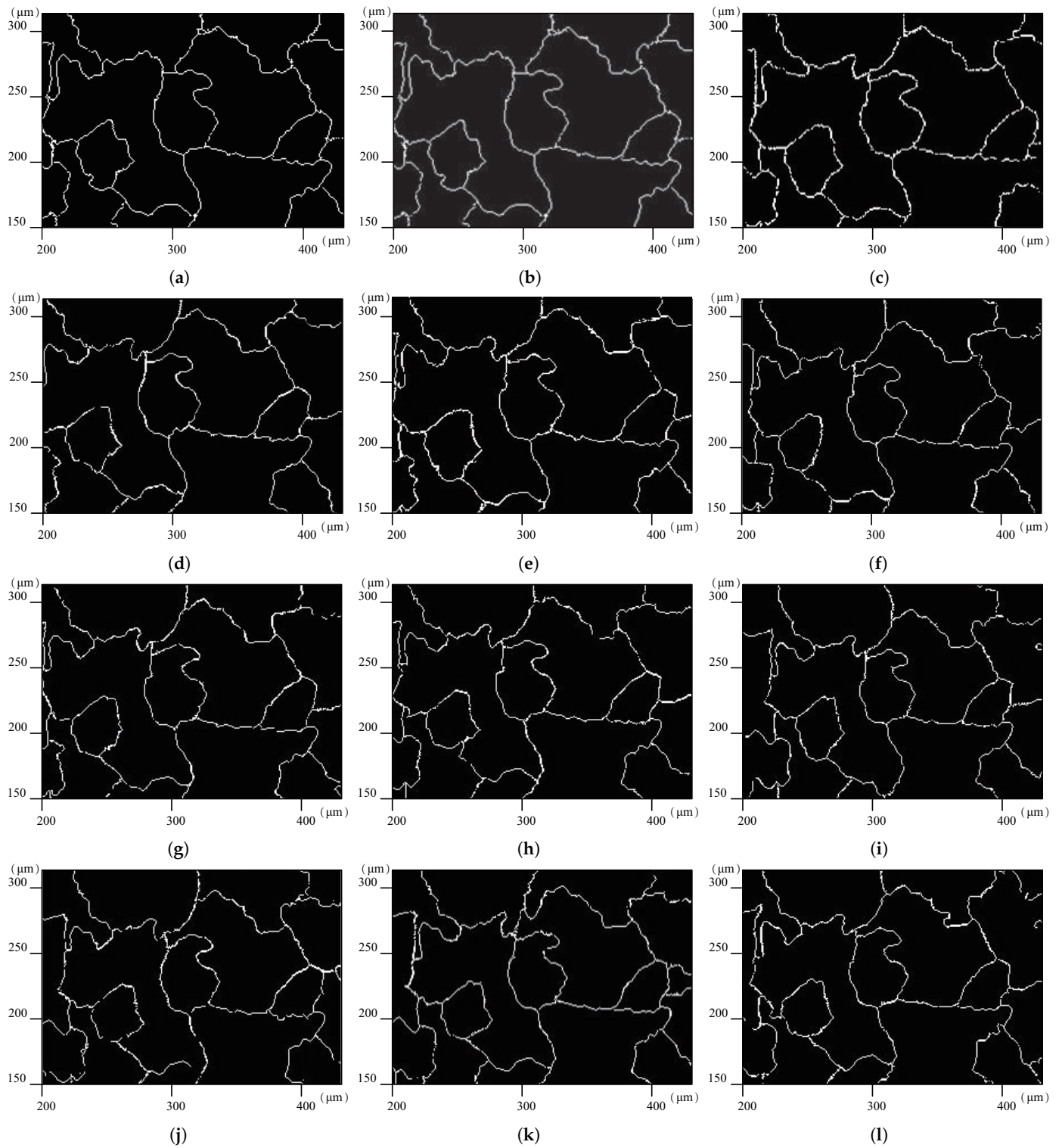
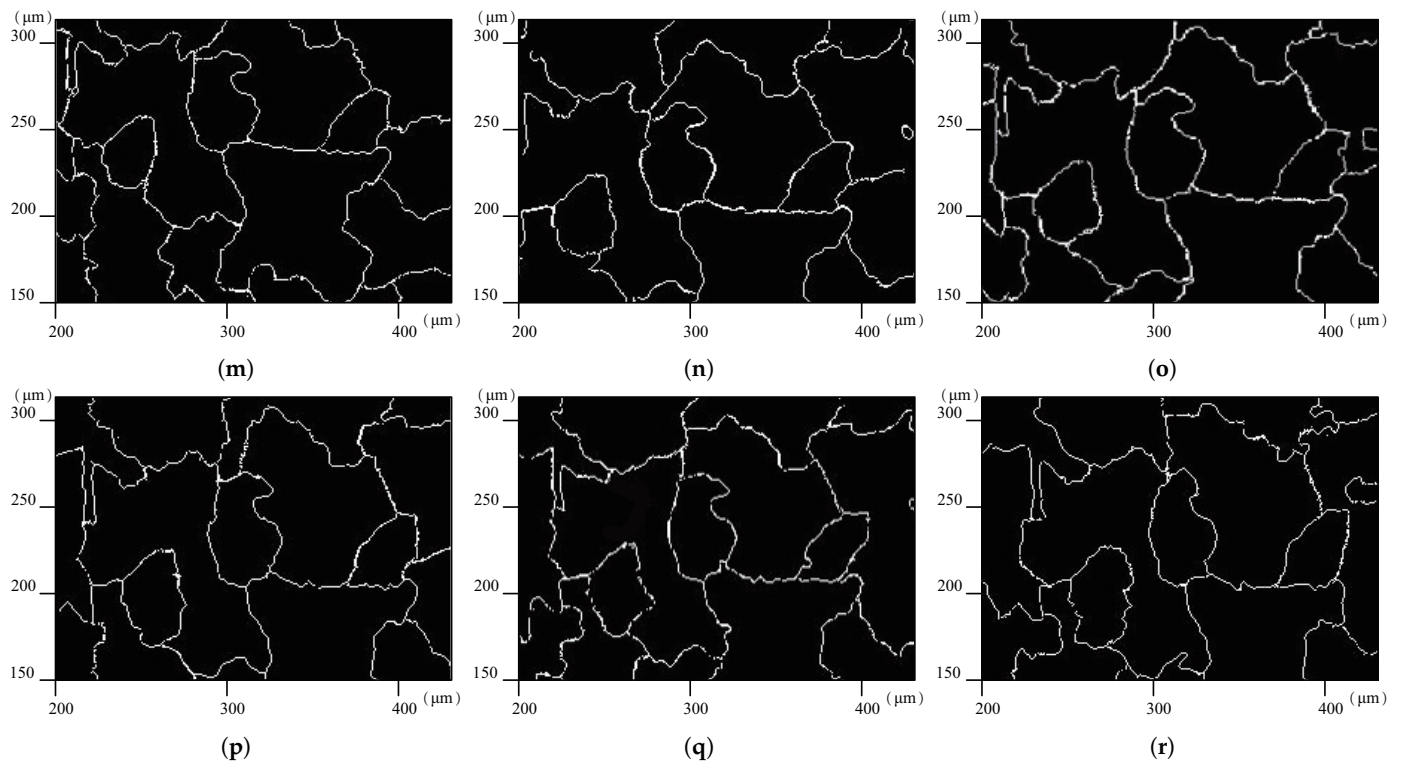


Figure 9. Cont.



**Figure 9.** The grain boundary observed under monotonically increasing tensile loading  $F$ : (a)  $F = 0$  N; (b)  $F = 200$  N; (c)  $F = 600$  N; (d)  $F = 1000$  N; (e)  $F = 1200$  N; (f)  $F = 1400$  N; (g)  $F = 1600$  N; (h)  $F = 1800$  N; (i)  $F = 2000$  N; (j)  $F = 2200$  N; (k)  $F = 2400$  N; (l)  $F = 2600$  N; (m)  $F = 2800$  N; (n)  $F = 3000$  N; (o)  $F = 3200$  N; (p)  $F = 3400$  N; (q)  $F = 3600$  N; (r)  $F = 3800$  N.

Since the shape of the target grain is close to the ellipse, according to Section 3, we use the seven chord method to fit, and take the slenderness ratio as the shape parameter of the grain to describe the shape of the target grain. The load of the target grain and the corresponding shape parameter (slenderness ratio) are shown in Table 6. Through comparative calculation, the fitting results of the seven chord method are very close.

**Table 6.** The load and corresponding shape parameters of target grain (slenderness ratio).

Load (N)	Shape Parameter	Load (N)	Shape Parameter	Load (N)	Shape Parameter
0	0.717802	1600	0.713215	2800	0.695813
200	0.721352	1800	0.720267	3000	0.67768
600	0.721482	2000	0.703568	3200	0.681628
1000	0.717047	2200	0.723909	3400	0.687682
1200	0.717419	2400	0.704046	3600	0.622458
1400	0.711743	2600	0.718436	3800	0.545502

Further, we obtain the relationship curve between the load of the target grain and the corresponding shape parameter (slenderness ratio), as shown in Figure 10.

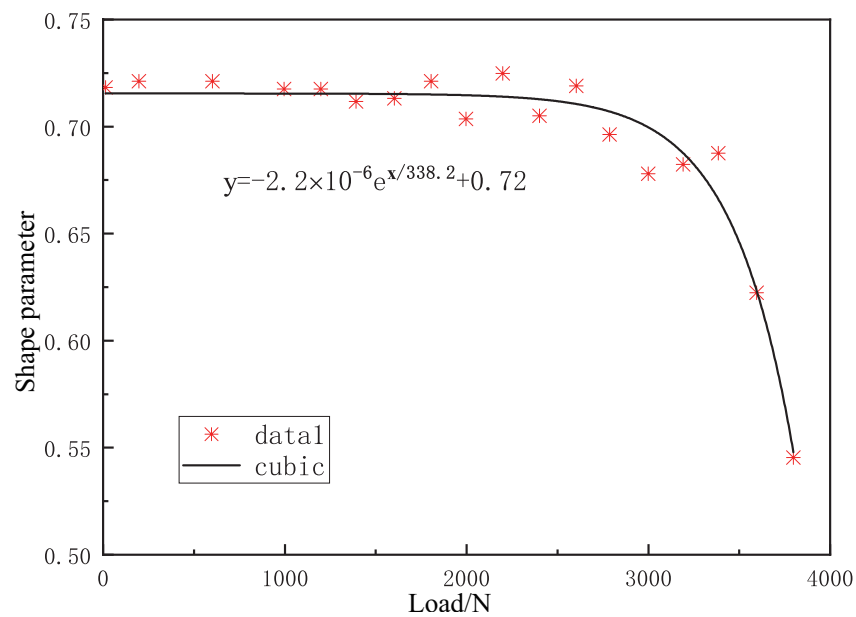


**Figure 10.** The relation curve between the load of target grain and corresponding shape parameter (slenderness ratio).

According to the results in Table 6 and Figure 10, the aluminum plate tensile process has gone through the elastic and plastic stages. In the elastic deformation stage, the load is less than 2500 N, and the shape parameters (slenderness ratio) of the selected target grains in the aluminum plate are between 0.70 and 0.72, basically keeping constant. When the load is greater than 2600 N, the aluminum plate enters the plastic deformation stage, and the slenderness ratio of the target grain becomes significantly smaller, and the slenderness ratio finally approaches 0.5. The experimental results of the shape evolution of a single typical grain are consistent with the theoretical results of the macroscopic mechanical properties of aluminum metal plates, e.g., the Poisson's ratio in the elastic phase is constant, and the volume of plastic deformation is constant, which also indicates that the experimental research based on grain size and digital image analysis technology in this paper reveals the relationship between the microscopic mechanical properties of grains and the macroscopic mechanical properties of metal plates.

## 5. Conclusions

1. Polycrystalline metallic materials are composed of small grains, and their constitutive relations must be related to the characteristics of grains, e.g., the average shape and orientation distribution of grains. According to the principle of no difference in the material frame, we choose the ratio of the arbitrary radius value in the grain to the average radius value of the grain, and establish the GSF, which can be used to describe the average shape of the grain. The GSF can be expanded into infinite series on the basis of Wigner D function, and the expanded coefficient is defined as the grain shape coefficient  $s_{m0}^l$ .
2. We discuss the shape coefficients of special grains with weak anisotropy, and obtain the expression of the shape coefficients. Considering the average grain shape effect, we study the elastic constitutive relation of metallic multi-grain materials, and derive the analytical formula of elastic constitutive relation containing the grain shape coefficient  $s_{m0}^l$ .
3. By using the power transformation, we improve the linear contrast of the digital image of the grain in polycrystalline metal materials, adopt the open and close operations in mathematical morphology to smooth the image, and then carry out histogram equalization and filtering noise removal processing to obtain a more ideal grain boundary. The approximate boundary of the image is extracted by the Canny operator, and then the boundary image is linearly expanded and refined. Then, using the internal

function of MATLAB, a single, complete grain with clear and accurate boundary is obtained, and a total of 15 grain images of three grains are extracted under five loading steps.

4. We discuss the mathematical description method of grain shape, and propose the multi-chord method to segment grains to represent the grain shape. When the grain shape is particularly irregular, the seven chord method is more reasonable. Furthermore, we carry out the experimental research on the shape function and shape coefficient of grains, fit the shape function of irregular grains, and prove that the shape function of grains can better describe the shape of irregular grains.
5. Using the digital image analysis method of grains (e.g., the grain boundary processing, grain image acquisition, and grain shape parameterization), we track the shape evolution of the target grains in the metal materials under stress, obtain the parameterized representation of grain deformation, and analyze the relationship between the metal materials' micro deformation and the materials' macro mechanical properties.

**Author Contributions:** Conceptualization, Z.L.; software, H.S. and M.H.; formal analysis, L.Z. and H.Y.; investigation, H.S.; resources, Z.L.; data curation, T.Z. and M.H.; writing—original draft preparation, Z.L. and T.Z.; writing—review and editing, T.Z. and Z.L.; project administration, Z.L. All authors have read and agreed to the published version of the manuscript.

**Funding:** This research was funded by the Jiangxi Province Education Science “14th Five-Year Plan” Project (Awards Nos. 22QN007) and the National Natural Science Foundation of China (Awards Nos. 51568046).

**Data Availability Statement:** The data of this study are available from the corresponding author upon request.

**Conflicts of Interest:** The authors declare no conflict of interest.

## References

1. Adams, B.L. Orientation imaging microscopy: Emerging and future applications. *Ultramicroscopy* **1997**, *67*, 11–17. [[CrossRef](#)]
2. Thakur, A.; Gangopadhyay, S. State-of-the-art in surface integrity in machining of nickel-based super alloys. *Int. J. Mach. Tools Manuf.* **2016**, *100*, 25–54. [[CrossRef](#)]
3. Veenhuizen, K.; McAnany, S.; Nolan, D.; Aitken, B.; Dierolf, V.; Jain, H. Fabrication of graded index single crystal in glass. *Sci. Rep.* **2017**, *7*, 44327. [[CrossRef](#)]
4. Pan, Q.; Yang, D.; Dong, G.; Qiu, J.; Yang, Z. Nanocrystal-in-glass composite (NGC): A powerful pathway from nanocrystals to advanced optical materials. *Prog. Mater. Sci.* **2022**, *130*, 100998. [[CrossRef](#)]
5. Trusov, P.; Kondratev, N.; Podsedertsev, A. Description of Dynamic Recrystallization by Means of An Advanced Statistical Multilevel Model: Grain Structure Evolution Analysis. *Crystals* **2022**, *12*, 653. [[CrossRef](#)]
6. Miller, A.K. *Unified Constitutive Equations for Creep and Plasticity*; Springer: Berlin/Heidelberg, Germany, 2012.
7. Walker, K.P. *Research and Development Program for Non-Linear Structural Modelling with Advanced Time-Temperature Dependent Constitutive Relationships*; NASA CR-165533, Report; National Aeronautics and Space Administration: Washington, DC, USA, 1981.
8. Bodner, S.R. *Unified Plasticity—An Engineering Approach (Final Report)*; Faculty of Mechanical Engineering, Technion-Israel Institute of Technology: Haifa, Israel, 2000; p. 32000.
9. Mahmoudi, A.H.; Pezeshki-Najafabadi, S.M.; Badnava, H. Parameter determination of Chaboche kinematic hardening model using a multi objective Genetic Algorithm. *Comput. Mater. Sci.* **2011**, *50*, 1114–1122. [[CrossRef](#)]
10. Sadovskii, V.M.; Sadovskaya, O.V.; Petrakov, I.E. On the theory of constitutive equations for composites with different resistance in compression and tension. *Compos. Struct.* **2021**, *268*, 113921. [[CrossRef](#)]
11. Feng, M.; Lu, H.; Lin, G.; Guo, Y. A unified visco-elastic-plastic constitutive model for concrete deformation. *Eng. Mech.* **2002**, *19*, 1–6. [[CrossRef](#)]
12. Man, C.S.; Du, W. Recasting Classical Expansion of Orientation Distribution Function as Tensorial Fourier Expansion. *J. Elast.* **2022**, 1–23. [[CrossRef](#)]
13. Xu, B.; Mao, N.; Zhao, Y.; Tong, L.; Zhang, J. Polarized Raman spectroscopy for determining crystallographic orientation of low-dimensional materials. *J. Phys. Chem. Lett.* **2021**, *12*, 7442–7452. [[CrossRef](#)]
14. Li, S.; Zhang, X.; Wang, C.; Jian, X. Texture evolution during uniaxial tension of aluminum sheet. *Chin. J. Nonferr. Met.* **1999**, *9*, 45–48.
15. Liu, W.C.; Man, C.S.; Morris, J.G. Lattice rotation of the cube orientation to the  $\beta$  fiber during cold rolling of AA 5052 aluminum alloy. *Scr. Mater.* **2001**, *45*, 807–814. [[CrossRef](#)]

16. Ivasishin, O.M.; Shevchenko, S.V.; Vasiliev, N.L.; Semiatinb, S.L. A 3-D Monte-Carlo (Potts) model for recrystallization and grain growth in polycrystalline materials. *Mater. Sci. Eng. A* **2006**, *433*, 216–232. [[CrossRef](#)]
17. Guenoun, G.; Schmitt, N.; Roux, S.; Régnier, G. Crystalline orientation assessment in transversely isotropic semicrystalline polymer: Application to oedometric compaction of PTFE. *Polym. Eng. Sci.* **2021**, *61*, 107–114. [[CrossRef](#)]
18. Tang, P.; Feng, J.; Wan, Z.; Huang, X.; Yang, S.; Lu, L.; Zhong, X. Influence of grain orientation on hardness anisotropy and dislocation behavior of AlN ceramic in nanoindentation. *Ceram. Int.* **2021**, *47*, 20298–20309. [[CrossRef](#)]
19. Şahin, K.; Clawson, J.K.; Singletary, J.; Horner, S.; Zheng, J.; Pelegri, A.; Chasiotis, I. Limiting role of crystalline domain orientation on the modulus and strength of aramid fibers. *Polymer* **2018**, *140*, 96–106. [[CrossRef](#)]
20. Tang, H.; Huang, H.; Liu, C.; Liu, Z.; Yan, W. Multi-Scale modelling of structure-property relationship in additively manufactured metallic materials. *Int. J. Mech. Sci.* **2021**, *194*, 106185. [[CrossRef](#)]
21. Gu, S.; Zhao, J.; Ma, T.; Xu, T.; Yu, B. Modeling and analysis of grain morphology effects on deformation response based on crystal plasticity finite element method. *Mater. Und Werkst.* **2022**, *53*, 770–780. [[CrossRef](#)]
22. Trusov, P.; Shveykin, A.; Kondratev, N. Some Issues on Crystal Plasticity Models Formulation: Motion Decomposition and Constitutive Law Variants. *Crystals* **2021**, *11*, 1392. [[CrossRef](#)]
23. Lakshmanan, A.; Yaghoobi, M.; Stopka, K.S.; Sundararaghavan, V. Crystal plasticity finite element modeling of grain size and morphology effects on yield strength and extreme value fatigue response. *J. Mater. Res. Technol.* **2022**, *19*, 3337–3354. [[CrossRef](#)]
24. Agius, D.; Kareer, A.; Al Mamun, A.; Truman, C.; Collins, D.M.; Mostafavi, M.; Knowles, D. A crystal plasticity model that accounts for grain size effects and slip system interactions on the deformation of austenitic stainless steels. *Int. J. Plast.* **2022**, *152*, 103249. [[CrossRef](#)]
25. Nabergoj, M.; Urevc, J.; Halilović, M. Function-based reconstruction of the fiber orientation distribution function of short-fiber-reinforced polymers. *J. Rheol.* **2022**, *66*, 147–160. [[CrossRef](#)]
26. Zhu, S.; Zhao, M.; Mao, J.; Liang, S.Y. Study on Hot Deformation Behavior and Texture Evolution of Aluminum Alloy 7075 Based on Visco-Plastic Self-Consistent Model. *Metals* **2022**, *12*, 1648. [[CrossRef](#)]
27. Zheng, C.; Xu, L.; Feng, X.; Huang, Q.; Li, Y.; Zhang, Z.; Yang, Y. Influence of Grain Orientation and Grain Boundary Features on Local Stress State of Cu-8Al-11Mn Alloy Investigated Using Crystal Plasticity Finite Element Method. *Materials* **2022**, *15*, 6950. [[CrossRef](#)] [[PubMed](#)]
28. Huang, Y. *A User-Material Subroutine Incorporating Single Crystal Plasticity in the ABAQUS Finite Element Program*; Harvard University: Cambridge, MA, USA, 1991.
29. Xiao, J.; Cui, H.; Zhang, H.; Wen, W.; Zhou, J. A physical-based constitutive model considering the motion of dislocation for Ni3Al-base superalloy. *Mater. Sci. Eng. A* **2020**, *772*, 138631. [[CrossRef](#)]
30. Zhang, M.; Zhang, J.; McDowell, D.L. Microstructure-based crystal plasticity modeling of cyclic deformation of Ti-6Al-4V. *Int. J. Plast.* **2007**, *23*, 1328–1348. [[CrossRef](#)]
31. Bandyopadhyay, R.; Mello, A.W.; Kapoor, K.; Reinhold, M.P.; Broderick, T.F.; Sangid, M.D. On the crack initiation and heterogeneous deformation of Ti-6Al-4V during high cycle fatigue at high R ratios. *J. Mech. Phys. Solids* **2019**, *129*, 61–82. [[CrossRef](#)]
32. Bridier, F.; McDowell, D.L.; Villechaise, P.; Mendez, J. Crystal plasticity modeling of slip activity in Ti-6Al-4V under high cycle fatigue loading. *Int. J. Plast.* **2009**, *25*, 1066–1082. [[CrossRef](#)]
33. Ma, A.; Dye, D.; Reed, R.C. A model for the creep deformation behaviour of single-crystal superalloy CMSX-4. *Acta Mater.* **2008**, *56*, 1657–1670. [[CrossRef](#)]
34. Rodas, E.A.E.; Neu, R.W. Crystal viscoplasticity model for the creep-fatigue interactions in single-crystal Ni-base superalloy CMSX-8. *Int. J. Plast.* **2018**, *100*, 14–33. [[CrossRef](#)]
35. Mori, T.; Tanaka, K. Average stress in matrix and average elastic energy of materials with misfitting inclusions. *Acta Metall.* **1973**, *21*, 571–574. [[CrossRef](#)]
36. Tandon, G.P.; Weng, G.J. The effect of aspect ratio of inclusions on the elastic properties of unidirectionally aligned composites. *Polym. Compos.* **1984**, *5*, 327–333. [[CrossRef](#)]
37. Mura, T. *Micromechanics of Defects in Solids (Mechanics of Elastic and Inelastic Solids)*; Kluwer Academic Publishers: Amsterdam, The Netherlands, 1987.
38. Benveniste, Y. A new approach to the application of Mori-Tanaka's theory in composite materials. *Mech. Mater.* **1987**, *6*, 147–157. [[CrossRef](#)]
39. Bunge, H.J. *Texture Analysis in Material Science: Mathematical Methods*; Butterworths: London, UK, 1982.
40. Huang, M.; Man, C.S. Constitutive relation of elastic polycrystal with quadratic texture dependence. *J. Elast.* **2003**, *72*, 183–212. [[CrossRef](#)]
41. Man, C.S. On the Constitutive Equations of Some Weakly-Textured Materials. *Arch. Ration. Mech. Anal.* **1998**, *143*, 77–103. [[CrossRef](#)]
42. Huang, M. Elastic constants of a polycrystal with an orthorhombic texture. *Mech. Mater.* **2004**, *36*, 623–632. [[CrossRef](#)]
43. Huang, M. Perturbation approach to elastic constitutive relations of polycrystals. *J. Mech. Phys. Solids* **2004**, *52*, 1827–1853. [[CrossRef](#)]